



Gaussian Process Model for the Local Stellar Velocity Field from *Gaia* Data Release 2

Patrick Nelson¹  and Lawrence M. Widrow¹ 

¹*Department of Physics, Engineering Physics, and Astronomy, Queen's University, Kingston, K7L 3N6, Canada*

Accepted XXX. Received YYY; in original form ZZZ

ABSTRACT

We model the local stellar velocity field using position and velocity measurements for 4M stars from the second data release of *Gaia*. We determine the components of the mean or bulk velocity in $\sim 27k$ spatially-defined bins. Our assumption is that these quantities constitute a Gaussian process where the correlation between the bulk velocity at different locations is described by a simple covariance function or kernel. We use a sparse Gaussian process algorithm based on inducing points to construct a non-parametric, smooth, and differentiable model for the underlying velocity field. We estimate the Oort constants A , B , C , and K and find values in excellent agreement with previous results. Maps of the velocity field within 2 kpc of the Sun reveal complicated substructures, which provide clear evidence that the local disk is in a state of disequilibrium. We present the first 3D map of the divergence of the stellar velocity field and identify regions of the disk that may be undergoing compression and rarefaction.

Key words: Galaxy: kinematics and dynamics – Galaxy: structure

1 INTRODUCTION

A common strategy for understanding the dynamics of the Milky way is to assume that phenomena such as the bar, spiral arms, and warp can be understood as perturbative departures from an equilibrium state (See, for example, [Binney \(2013\)](#); [Sellwood \(2013\)](#)). A further assumption is that stars orbit in the mean gravitational field of gas, dark matter, and the other stars. The stellar components of the Galaxy are then described by a phase space distribution function (DF), $f(\mathbf{x}, \mathbf{v}, t)$, which obeys the collisionless Boltzmann equation (CBE) coupled to gravity via Poisson's equation. The equilibrium/perturbation split then carries over to the DF and gravitational potential Ψ . For a disk galaxy such as the Milky Way, the equilibrium state exhibits symmetry about both the its midplane and rotation axis. Any departure from these symmetries therefore signals a departure from equilibrium.

The second *Gaia* data release (*Gaia* DR2, [Gaia Collaboration et al. \(2018\)](#)) includes measurements of positions and velocities for over seven million stars thereby vastly increasing the number of stars for which all phase space coordinates are known. This data provides an estimate of the present-day stellar DF near the Sun in the sense that each star can be represented as a phase space probability distribution function P_i that reflects observational uncertainties in its position and velocity:

$$f(\mathbf{x}, \mathbf{v}, t) = \sum_i P_i(\mathbf{x} - \mathbf{x}_i, \mathbf{v} - \mathbf{v}_i) . \quad (1)$$

In the limit of perfect observations, P_i reduces to a six-dimensional

delta function. In general, interpretation of the DF involves the construction of a set of observables

$$O = \int d^3x' d^3v' f(\mathbf{x}', \mathbf{v}', t) \mathcal{F}(\mathbf{x}', \mathbf{v}') \quad (2)$$

where \mathcal{F} is designed to pick out particular features of the DF and also account for the selection function of the survey. For example, an estimate of the number density $n(\mathbf{x})$ is obtained by setting $\mathcal{F} = \mathcal{W}(\mathbf{x} - \mathbf{x}')$ where \mathcal{W} is a localized window function:

$$n(\mathbf{x}) = \int d^3x' d^3v' f(\mathbf{x}', \mathbf{v}', t) \mathcal{W}(\mathbf{x} - \mathbf{x}') . \quad (3)$$

In this paper, we focus on the first velocity moment of the DF:

$$\mathbf{V}(\mathbf{x}) = n^{-1} \int d^3x' d^3v' f(\mathbf{x}', \mathbf{v}', t) \mathcal{W}(\mathbf{x} - \mathbf{x}') \mathbf{v} . \quad (4)$$

For a system in equilibrium, \mathbf{V} is a function of Galactocentric radius R and distance from the midplane $|z|$.

Studies of the bulk velocity in pre-*Gaia* surveys such as the Sloan Extension for Galactic Understanding and Exploration (SEGUE) ([Yanny et al. 2009](#)), the Radial Velocity Experiment (RAVE) ([Steinmetz et al. 2006](#)), and Large Sky Area Multi-Object Fiber Spectroscopic Telescope (LAMOST) ([Cui et al. 2012](#)) revealed bulk motions than signaled a Galaxy in disequilibrium. For example, [Widrow et al. \(2012\)](#) determined the bulk vertical velocity V_z and its dispersion σ_z as functions of z for SEGUE stars and found that they showed features asymmetric about $z = 0$. [Williams et al. \(2013\)](#) determined the full 3D velocity field from some 70k red clump stars in the RAVE survey and found vertical motions that varied with Galactocentric radius R as well as evidence for radial flows. Similarly, [Carlin et al. \(2013\)](#) and [Pearl et al. \(2017\)](#) used LAMOST spectroscopic velocities with proper motions from the PPMXL catalog ([Roesser et al.](#)

★ E-mail: patrick.nelson@queensu.ca

† E-mail: widrow@queensu.ca

2010) for 400k stars to map out both vertical and radial bulk motions. Finally, Schönrich et al. (2019) and Friske & Schönrich (2019) found a wavelike pattern in the mean vertical velocity as a function of angular momentum about the spin axis of the Galaxy, which served as a proxy for Galactocentric radius.

Unfortunately, a clear picture of bulk motions near the Sun from these and other studies never emerged. The surveys each had their own complicated selection functions, as illustrated in Figure 1 of Carlin et al. (2013). Furthermore, systematic distance errors could masquerade as velocity-space substructure (Schönrich 2012; Carrillo et al. 2018). These problems were alleviated by Katz, D. et al. (2019) who presented a series of velocity field maps using data from *Gaia* DR2 and straight-forward binning procedures. For example, they constructed face-on maps by first dividing the sample into vertical slabs of width $\Delta z = 400$ pc and then computing the mean velocity in xy -cells of 200 pc by 200 pc. Similar binning procedures were used to construct maps of the velocity field in the $R - z$ and $R - \phi$ planes.

The *Gaia* kinematic maps are simple and intuitive though the connection with theory, say through the CBE, requires further analysis. In particular, the mean velocities in the *Gaia* maps differ from the moments that appear in the continuity and Jeans equations since the former are averaged over cells of a finite size that must strike a balance between improved spatial resolution and reduced statistical fluctuations. The situation is only exacerbated when one goes to compute gradients of the velocity field.

In this paper, we take a different approach based on Gaussian process (GP) regression, a Bayesian, (almost) nonparametric approach to fitting data from the field of machine learning (See, for example, Rasmussen & Williams (2006)). GP regression has been used extensively in data science and engineering though only recently has it been applied to problems in astrophysics. An example that has some similarities with the problem at hand is the construction of dust and extinction maps in the Galaxy (see, for example, Sale & Magorrian (2018)). (For a different approach for constructing smooth maps of streaming motions, see Khanna et al. (2022).)

Our provisional starting point is the assumption that the velocities of stars in the Galaxy constitute, to a good approximation, a Gaussian process. Formally, a Gaussian process is a collection of random variables such that any subset of these variables is Gaussian. Stellar velocities would seem to be a good candidate for a GP since the velocity distributions for the different stellar components (thin and thick disks, stellar halo) are well-described by anisotropic Maxwellians (Binney & Tremaine 2008).

The fundamental object in GP regression is the covariance matrix, which describes correlations in the output variables for different values of the inputs. In our case, the outputs are the components of the velocity field and the inputs are different positions within the Galaxy. The covariance matrix is constructed from a kernel function, which depends of a set of hyperparameters that control the strength and scale length of correlations in the velocity field. Thus, although the model for the velocity field itself is nonparametric, the covariance function is parametric. The driver in GP regression is optimization of the likelihood function, defined below, over the space of hyperparameters. Note that GP regression is different from kernel smoothing or kernel density estimation, where one produces a smooth model by convolving the data with a window function. In GP regression, we use the data to select a model from the space of nonparametric functions in the GP prior.

To evaluate the GP likelihood function, one must invert an N by N covariance matrix where N is the number of observations. This calculation is an $O(N^3)$ operation that requires $O(N^2)$ rapid-access memory (RAM) capabilities. Clearly, it is unfeasible to apply GP

regression directly to the *Gaia* data, where N in DR2 already exceeds 10^6 . In this work, we apply a two-fold strategy for handling the large- N bottleneck. First, we bin stars into cells of size $(\Delta x, \Delta y, \Delta z) = (125, 125, 50)$ pc. The factor of 2.5 difference in Δz is meant to account for the difference between the radial scale length and the vertical scale height of the disk. Note that the width of the bins in z are a factor of 8 smaller than those used in constructing the Katz, D. et al. (2019) face-on maps. Our binning procedure leads to roughly 27k cells above our threshold of 20 stars. We then use a sparse GP algorithm that deploys M inducing points to approximate the likelihood function. This algorithm reduces the computational complexity to $O(NM^2)$ and the RAM requirements to $O(NM)$.

Our GP analysis leads to a single model from which other properties of the velocity field can be derived. By contrast Katz, D. et al. (2019) use different binning strategies to explore different facets of the velocity field. Moreover, the *Gaia* maps are somewhere between a projection, where one integrates out one spatial dimension, and a two-dimensional slice, where one takes a narrow range in one of the dimensions to get the velocity field on a two-dimensional surface. By contrast, our GP model can be queried to give the inferred velocity field with uncertainties at any point in the sample region. Furthermore, since the model is differentiable, We can use it to infer quantities such as the Oort constants at the position of the Sun. In addition, derivatives of \mathbf{V} can be used to make statements about the dynamical state of the Galaxy. This feature allows us to map out variations in Oort functions in the vicinity of the Sun. It also allows us to construct a 3D map of the divergence, which is proportional to the total time derivative of the stellar number density. In so doing, we are able to identify regions near the Sun where the number density of stars may be undergoing compression and rarefaction.

An outline of our paper is as follows. In Section 2 we describe the sample used in our analysis as well as our binning strategy. In Section 3 we provide a brief introduction to Gaussian processes and outline our sparse GP algorithm. We also summarize results of tests performed with mock data. The results of our analysis for *Gaia* DR2 are discussed in Sections 4 and 5. We present estimates for the generalized Oort constants and maps of the velocity field as well as a three-dimensional map of the divergence of the velocity field. We discuss possible extensions of this work in Section 6 and provide a brief summary of our results and some concluding remarks in Section 7.

2 PRELIMINARIES

2.1 6D phase space catalog

The *Gaia* DR2 Radial Velocity survey contains 6D phase-space measurements for over 7 million stars (Gaia Collaboration et al. 2018; Katz, D. et al. 2019). In this work, we use the *gaiaRVdelpepsdelspl43* catalog, which was constructed to correct for systematic errors in the *Gaia* parallaxes and uncertainties (Schönrich et al. 2019)¹.

Following Katz, D. et al. (2019) we use both Cartesian coordinates (X, Y, Z, U, V, W) and Galactic cylindrical coordinates $(R, \phi, Z, V_R, V_\phi, V_Z)$. The Cartesian coordinate system has the Galactic centre at the origin and the Sun on the $-X$ -axis; U, V and W are the usual velocity components where positive values at the position of the Sun indicate motion toward the Galactic centre, the direction of Galactic rotation, and the North Galactic Pole, respectively. We use 8.27 kpc for the Sun's distance

¹ See <https://doi.org/10.5281/zenodo.2557803>

to the Galactic centre and 20 pc for its distance to the Galactic midplane (see Schönrich et al. (2019) and references therein) so that $(X_\odot, Y_\odot, Z_\odot) = (-8.27, 0, 0.02)$ kpc. We further set $(U_\odot, V_\odot, W_\odot) = (11.1, 250, 7.24)$ km s⁻¹ (Schönrich 2012). Our cylindrical coordinate system also has the Galactic centre at the origin, the Sun at $\phi = 0^\circ$, and ϕ increasing in the direction of Galactic rotation. This system is left-handed in the sense that increasing ϕ corresponds to the direction toward the South rather than North Galactic pole. We note that at the position of the Sun $V_R = -U$ and $V_\phi = V$; $V_Z = W$.

We calculate the U, V, W velocity components and their errors from astrometric observations using the method described in Johnson & Soderblom (1987). We then convert to V_R, V_ϕ and V_Z . The velocity components, but not their errors, were provided with the *gaiaRVdelpepsdelp43* catalog. Note that in that catalog, the Galactocentric cylindrical velocity components were given as $(U_g, V_g, W_g) = (-V_R, V_\phi, V_Z)$ and the Cartesian coordinates were given as $(x, y, z) = (-X, Y, Z)$.

We apply the following restrictions to the sample:

- color: $G_{bp} - G_{rp} < 1.5$
- magnitude: $G < 14.5$ and $G_{bp}, G, G_{rp} > 0$
- parallax signal to noise: $p/\sigma_p > 4$
- parallax uncertainty: $\sigma_p < 0.1$ mas with σ_p given by the *Gaia* pipeline
- excess $B - R$ flux: $1.172 < E_{bprp} < 1.3$

These quality cuts are recommended in Schönrich et al. (2019) to ensure minimal systematic biases in derived kinematic quantities. They leave 4584106 stars from the original catalog of 6606247. Finally, we apply the following kinematic cuts to remove high-velocity outliers:

- proper motion: $\mu_\alpha, \mu_\delta < 400$ mas yr⁻¹
- proper motion error: $\epsilon_{\mu_\alpha}, \epsilon_{\mu_\delta} < 20$ mas yr⁻¹
- Galactocentric speed: $|\mathbf{V}| < 600$ km s⁻¹

These cuts are similar to those implemented by Williams et al. (2013) with the modification that our velocity cut is in terms of the speed in the local frame of rest whereas they apply a cut on the radial velocity. These cuts eliminate only about 400 stars.

2.2 Binning

As discussed above, computation time and RAM requirements make it unfeasible to apply GP regression directly to data sets with much more than 10^4 entries. For this reason, we bin stars so that input data for our GP analysis are the mean velocity components in cells. In a sense, velocity components averaged over stars in a cell are closer to Gaussian process than the stellar velocities themselves. Stars in the region near the Sun can come from the thin disk, the thick disk, or the stellar halo. The velocity distributions for these components are roughly Maxwellian. Thus, the stellar velocities are drawn from what might be better described as a mixture of Gaussians. On the other hand, the average velocity of some large number of stars in a cell will be approximately Gaussian due to the central limit theorem.

We set up a Cartesian grid of cells with size $(\Delta x, \Delta y, \Delta z) = (125, 125, 50)$ pc for the region $4 < X(\text{kpc}) < 12, -4 < Y(\text{kpc}) < 4$, and $-2 < Z(\text{kpc}) < 2$ and keep only those cells with more than 20 stars. Mean values and uncertainties for the V_R, V_ϕ , and V_Z components are then calculated by a standard least squares algorithm. In the end, we are left with mean velocities for 27305 cells representing the observations of 3972825 stars.

3 GAUSSIAN PROCESS REGRESSION

3.1 Overview of Gaussian processes

We begin with a brief review of GP regression. More thorough discussions can be found in numerous resources such as the excellent book by (Rasmussen & Williams 2006). Suppose we have observations of a real scalar process f such that

$$y_i = f(\mathbf{x}_i) + \epsilon_i \quad i = \{1, 2, \dots, N\} \quad (5)$$

where \mathbf{x}_i is the input vector for the i 'th observation, y_i is the scalar output and ϵ_i is additive noise for that observation. For the case at hand, $\mathbf{x}_i = (X_i, Y_i, Z_i)$ is the position vector of the i 'th cell and f is V_R, V_ϕ , or V_Z . If f is a Gaussian Process then it is completely specified by a mean function $m(\mathbf{x})$ and covariance function $k(\mathbf{x}, \mathbf{x}')$ such that

$$m(\mathbf{x}) = \mathbb{E}[f(\mathbf{x})] \quad (6)$$

$$k(\mathbf{x}, \mathbf{x}') = \mathbb{E}[(f(\mathbf{x}) - m(\mathbf{x}))(f(\mathbf{x}') - m(\mathbf{x}'))] \quad (7)$$

where \mathbb{E} denotes expectation value. Furthermore, the probability distribution function of $\mathbf{f} \equiv [f_1, \dots, f(\mathbf{x}_n)]$ is given by

$$P(\mathbf{f} | \mathbf{X}) = \mathcal{N}(\mathbf{f} | \boldsymbol{\mu}, \mathbf{K}) \quad (8)$$

where \mathbf{X} , $\boldsymbol{\mu}$, and \mathbf{K} are aggregate vectors of the input vectors \mathbf{x}_i , the mean functions $m_i \equiv m(\mathbf{x}_i)$, and the kernel functions $K_{ij} \equiv k(\mathbf{x}_i, \mathbf{x}_j)$, respectively. As usual, \mathcal{N} denotes a multivariate Gaussian. Equation 8 constitutes a Gaussian process prior on f . For simplicity, we assume $m = 0$.

The goal of GP regression is to infer \mathbf{f}_* at new inputs \mathbf{X}_* given the data $\{\mathbf{X}, \mathbf{y}\}$. If the noise ϵ is identical, independent, and Gaussian with dispersion σ_n , then the joint probability for \mathbf{y} and \mathbf{f}_* is itself Gaussian

$$P(\mathbf{y}, \mathbf{f}_* | \mathbf{X}, \mathbf{X}_*) = \mathcal{N}\left(0, \begin{bmatrix} \mathbf{K} + \sigma_n^2 \mathbf{I} & \mathbf{K}_* \\ \mathbf{K}_*^T & \mathbf{K}_{**} \end{bmatrix}\right), \quad (9)$$

where $\mathbf{K} \equiv K(\mathbf{X}, \mathbf{X})$, $\mathbf{K}_* \equiv K(\mathbf{X}, \mathbf{X}_*)$ and $\mathbf{K}_{**} \equiv K(\mathbf{X}_*, \mathbf{X}_*)$. The quantity of interest is the conditional probability

$$P(\mathbf{f}_* | \mathbf{y}, \mathbf{X}, \mathbf{X}_*) = \frac{P(\mathbf{y}, \mathbf{f}_* | \mathbf{X}, \mathbf{X}_*)}{P(\mathbf{y})} \quad (10)$$

$$= \mathcal{N}(\bar{\mathbf{f}}_*, \mathbf{C}) \quad (11)$$

where

$$\bar{\mathbf{f}}_* = \mathbf{K}_*^T (\mathbf{K} + \sigma^2 \mathbf{I})^{-1} \mathbf{y} \quad (12)$$

and

$$\mathbf{C} = \mathbf{K}_{**} - \mathbf{K}_*^T (\mathbf{K} + \sigma^2 \mathbf{I})^{-1} \mathbf{K}_* \quad (13)$$

(see Rasmussen & Williams (2006), section 2.2 and appendix A).

3.2 Kernel function

A key ingredient of GP regression is the kernel or covariance function. Though there is considerable flexibility in choosing a kernel, for most problems it is constructed by taking sums and/or products of standard kernels, which themselves are constructed from elementary functions of the input variables.

In the present analysis, we allow for different kernels for V_R, V_ϕ , and V_Z since they are modeled as independent scalar functions. Each of the kernels uses a three-dimensional radial basis function (RBF)

plus a term proportional to the identity matrix that accounts for unknown noise

$$k(\mathbf{x}_i, \mathbf{x}_j) = \sigma_f^2 e^{-\tilde{r}_{ij}^2/2} + \sigma_n^2 \delta_{ij} \quad (14)$$

where σ_f^2 is the signal variance and

$$\tilde{r}_{ij} \equiv \frac{(X_i - X_j)^2}{l_x^2} + \frac{(Y_i - Y_j)^2}{l_y^2} + \frac{(Z_i - Z_j)^2}{l_z^2} \quad (15)$$

is a dimensionless pseudo-distance between \mathbf{x}_i and \mathbf{x}_j . The RBF kernel is positive definite, differentiable, and maximal for $\mathbf{x}_i = \mathbf{x}_j$. These are all features that lead to realistic models for the bulk velocity field of the Galactic disk. Through trial and error, we find that the fit for V_ϕ is significantly improved by including in k the product of two linear kernels. The linear kernel is given by

$$k_{\text{lin}}(\mathbf{x}, \mathbf{x}') = \sum_{i=x,y,z} \mu_i x_i x'_i. \quad (16)$$

It expands the space of priors on f to include linear functions of the inputs \mathbf{x} . Unlike the RBF kernel, it is non-stationary in the sense that it depends on the absolute positions of the data points rather than the distance between pairs of data points. For V_ϕ , we add

$$k_{\text{lin}2} = \left(\sum_{i=x,y,z} \mu_i x_i x'_i \right) \left(\sum_{j=x,y,z} \nu_j x_j x'_j \right) \quad (17)$$

to the RBF and noise kernels in Equation 14.

The kernels defined above depend on a number of free parameters commonly referred to as hyperparameters, since they parameterize the covariance function rather than f itself. The hyperparameters determine characteristics of functions in the prior of f . For example, l_x , l_y , and l_z control the correlation lengths along the three coordinate axes. Proper choice of hyperparameters is crucial for obtaining a good model of the data. If the length scales are too small, then the model will tend to overfit the data, thereby attributing small-scale bumps and wiggles to f rather than noise. Conversely, if the length scales are too large, then the model will tend to miss important features represented in the data.

In very simple problems, one can find suitable hyperparameters by trial and error as illustrated in Chapter 2 of [Rasmussen & Williams \(2006\)](#). A principled approach, and one that is suitable for more complex problems, is to maximize the marginal likelihood function $p(\mathbf{y}|\mathbf{X}, \theta)$ where

$$\log(p(\mathbf{y}|\mathbf{X}, \theta)) = -\frac{n}{2} \log(2\pi) - \frac{1}{2} \log |K + \sigma_n^2 I| - \frac{1}{2} \mathbf{y}^T (K + \sigma_n^2 I)^{-1} \mathbf{y}. \quad (18)$$

Here, θ represents the hyperparameters.

3.3 Sparse GP regression via inducing points

In any optimization scheme, one must evaluate the marginal likelihood function in Equation 18 a large number of times for different choices of the hyperparameters θ . Each likelihood call involves inversion of the $N \times N$ matrix K , which is an $O(N^3)$ operation that requires $O(N^2)$ RAM. This process becomes unfeasible for N much greater than 10^4 . Fortunately, there are a number of algorithms that allow one to estimate the marginal likelihood using $M < N$ inputs. These algorithms, generally referred to as sparse GP regression, reduce the computational complexity to $O(NM^2)$ and the RAM requirement to $O(NM)$. In this work, we follow the method described in ([Bauer](#)

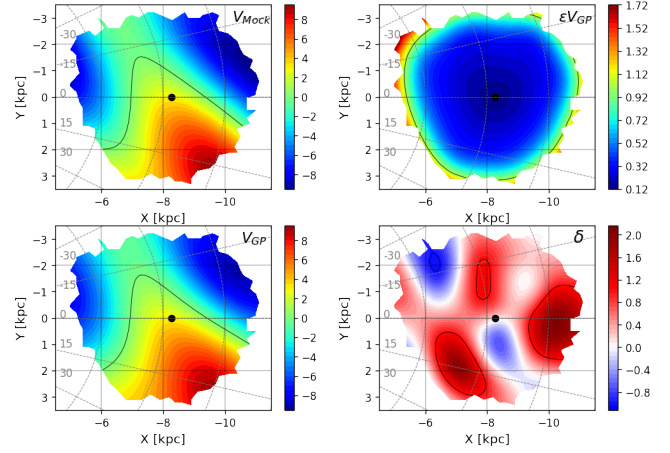


Figure 1. Results of a mock data test. Top left: the GP fit of the mock data. Top right: the confidence region of the model. Bottom left: the generating field for the mock data. Bottom right: the difference between the mock field and the model, scaled by the dispersion as calculated in the GP regression. Here and throughout, the black dot indicates the position of the Sun and velocities are given in km s^{-1} .

[et al. 2016](#)). We denote the full covariance matrix (\mathbf{K} in Equation 8) as \mathbf{K}_{ff} , the covariance matrix for the inducing points as \mathbf{K}_{uu} and the cross covariance matrix as \mathbf{K}_{fu} . In sparse GP regression, one replaces \mathbf{K}_{ff} in Equation 18 with $\mathbf{Q}_{ff} \equiv \mathbf{K}_{fu} \mathbf{K}_{uu}^{-1} \mathbf{K}_{uf}$ and includes an additional term given by $\text{Tr}(\mathbf{K}_{ff} - \mathbf{Q}_{ff}) / 2\sigma_n^2$ ([Titsias 2009](#); [Bauer et al. 2016](#)). Note that optimization requires that we compute the gradient of the marginal likelihood with respect to the hyperparameters.

We implement our GP algorithm using GPY, a Gaussian process package written in PYTHON by the University of Sheffield machine learning group ([GPY 2012](#)). We apply the sparse GP module with a heteroscedastic Gaussian likelihood, which allows us to incorporate uncertainties in the mean velocity components for individual cells. Optimization is carried out by applying the VARDTC inference method ([Titsias 2009](#)) using the GPY optimization module and the L-BFGS-B algorithm from the software package SCIPY ([Jorge Nocedal 2006](#); [Virtanen et al. 2020](#)).

3.4 Mock data tests

Before turning to *Gaia* DR2, we test our algorithm on a mock data sample. This sample is constructed by replacing measured velocities in the *gaiaRVdelpepsdelsp43* catalog with velocities drawn from an analytic function that is chosen so that the resulting maps are qualitatively similar to ones found with the real data. For brevity, we present results for a single generic component with velocity field. The analytic function is given by

$$V(X, Y, Z) = 2 \left(11 \cos g_1 - 3 \cos g_2 - 2 \cos g_3 - Z^2 - 10 \right) \quad (19)$$

where $g_1 = Z + (X - 8)/6$, $g_2 = 0.52(Y - 2)$, and $g_3 = X - 1.3Y - 11.3$. The velocity field for $Z = 0$ is shown in the upper left panel of Figure 1.

The mock data is analysed using the same procedure that will be applied to the real data. We first determine mean values for V and errors about the mean for the 27k cells. We then optimize the likelihood function over the hyperparameters using the inducing point algorithm described above with $M = 3000$ and the RBF plus noise kernel function. Armed with optimal hyperparameters, we determine

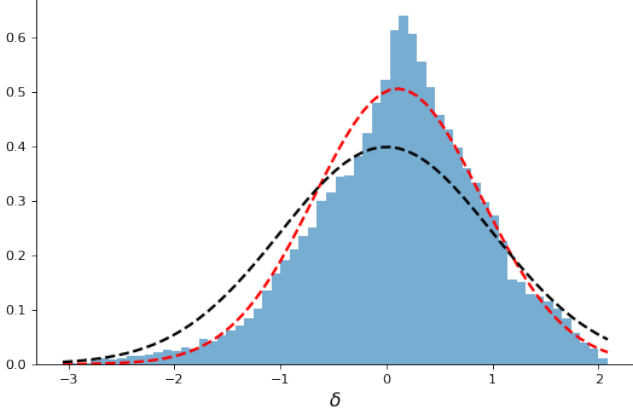


Figure 2. Histogram of the normalized residual δ as defined in the text. The histogram includes residuals from all cells used in fitting the mock data and is itself normalized so that the area under the curve is unity. The black dashed line is the normal distribution $\mathcal{N}(0, 1)$. The red dashed line is the normal distribution fit $\mathcal{N}(0.11, 0.79)$.

Table 1. Optimal hyperparameters from our sparse GP analysis of *Gaia* data. Units are kpc for l_i , km s^{-1} for σ_f and $\text{km s}^{-1} \text{kpc}^{-2}$ for μ_i and ν_i .

	V_R	V_ϕ	V_z
Kernel	RBF	RBF + lin2	RBF
l_x	1.06	1.13	1.89
l_y	2.72	1.75	4.18
l_z	0.536	0.242	0.484
σ_f	12.4	10.4	3.31
μ_x, ν_x		0.236, 0.228	
μ_y, ν_y		0.207, 0.209	
μ_z, ν_z		3.86, 3.71	

the posterior of the model velocity field $\tilde{\mathbf{V}}$ using Equation 12. The result for the XY -plane is shown in the lower left panel of Figure 1. We also determine the covariance matrix of the posterior using Equation 13. The square root of its diagonal elements provides an estimate of the dispersion, ϵ_V , which is shown in the upper right panel of Figure 1. As expected, the dispersion rises sharply toward the edges of the region where we have data. Finally, we show the normalized residual $\delta \equiv (V - \tilde{V})/\epsilon_V$ in the XY plane. In Figure 2, we plot a histogram of δ over the sample volume. If the agreement between model and mock data were perfect, we would expect the histogram to be well-approximated by the normal distribution, $\mathcal{N}(0, 1)$. Instead, we find that the histogram is fit by the Gaussian $\mathcal{N}(0.11, 0.79)$. This indicates that systematic errors are roughly a factor of 10 smaller than statistical ones and that uncertainties are over-estimated by $\sim 20\%$. Given that mock data was drawn from an analytic function rather than one generated from the GP prior, these small discrepancies are not unexpected.

4 RESULTS

As with the mock data, we analyse the *Gaia* DR2 sample by first determining the mean values and uncertainties for the three velocity components in our 27k cells. Hyperparameters from our optimization of the likelihood function are given in Table 1. We see that $l_y/l_x \sim 1.5 - 2.5$ and $l_x/l_z \sim 2 - 5$. The hierarchy of scales is expected given

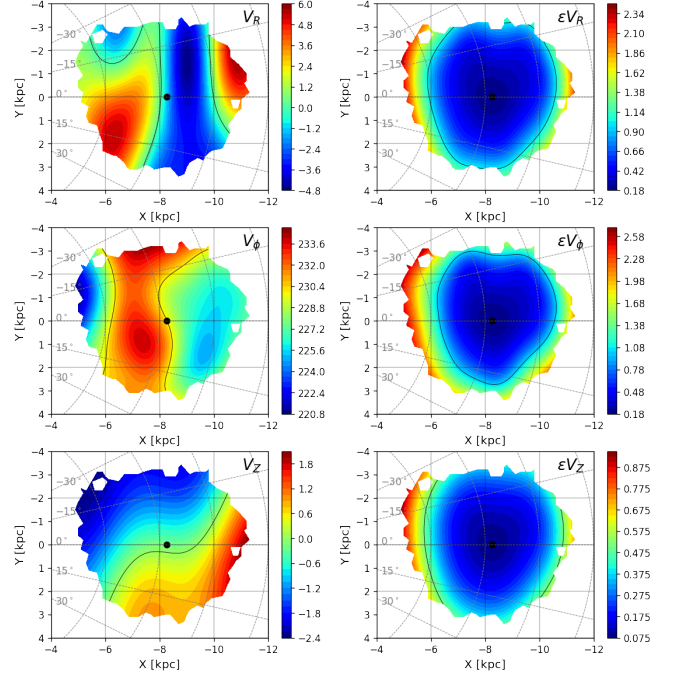


Figure 3. Left: Components of the velocity field V_R , V_ϕ , and V_z in the $z = 0$ plane. Right: One-sigma confidence regions of the GP models.

that the radial length scale of the disk is a factor of 5 – 10 times larger than the scale height and that variations in the disk tend to be stronger in the radial direction than the azimuthal direction.

4.1 Velocity field in components

Figures 7 and 6 show model predictions for the velocity field in the $z = 0$ and $\phi = 0^\circ$ planes. These figures are produced by querying the model at the appropriate points using Equation 12. By and large, the maps are in good agreement with those found in Katz, D. et al. (2019) (See their Figures 10 and 11) though they are clearly much smoother. The GP analysis tends to pick out features on the length scales characterized by l_x , l_y , and l_z . We also show the statistical uncertainties in the mean for the three components, ϵ_i , as calculated from Equation 13. In general the uncertainties are less than 1 km s^{-1} within the sample volume, but rise rapidly as one approaches the edge of the volume. Our maps can also be compared to those in Khanna et al. (2022) who combine data from *Gaia* EDR3 with radial velocity measurements from a number of spectroscopic surveys. They construct parametric models of the velocity field in heliocentric coordinates so a direct comparison is difficult.

The upper left panels of Figures 3 and 4 point to several regions of radial bulk flows. In particular, there is inward bulk motion just beyond the Solar circle that is approximately independent of ϕ across the sample volume. This motion is primarily in the region $|z| < 500 \text{ pc}$ and is thus likely associated with the thin disk. On the other hand, the outward radial flow just inside the Solar circle is mainly found at positive ϕ but across the full range in z of the survey. There also appears to be another outward flow at $R > 10 \text{ kpc}$, $\phi \approx -10^\circ$ and positive z .

The middle-left panels of Figures 3 and 4 show V_ϕ . The dominant flow here, and indeed for \mathbf{V} in general, is the motion about the Galactic centre. We see that contours of constant V_ϕ roughly follow contours

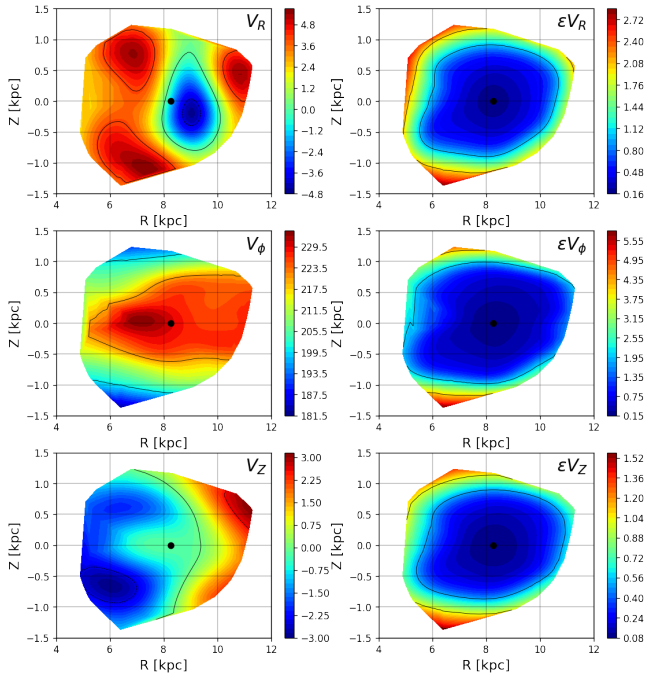


Figure 4. Left: Components of the velocity field in the $\phi = 0$ plane. Right: One-sigma confidence regions of the GP models.

of constant R in Figure 7. As discussed below, the average of V_ϕ over ϕ at $z = 0$ yields the rotation curve near the Solar circle. The main feature in Figure 4 is a decrease of V_ϕ as one moves away from the midplane of the Galaxy. This trend is easily explained by an increase in asymmetric drift due to a larger contribution from dynamically warmer stars in the thick disk. As with V_R , we see that V_ϕ is not perfectly symmetric about the midplane. Consider, for example, the ridge in V_ϕ between $X = -6$ and $X = -8$ in Figure 7, which coincides with the peak seen in Figure 6 at $R = 7$ kpc. The peak and its outer slopes are shifted by a small, but non-negligible, amount above the midplane.

The bottom left panels of Figures 3 and 4 show our results for the vertical bulk motion, V_Z . In the midplane we see a clear trend of increasing V_Z as one moves across the local patch of the Galaxy in the direction of increasing R and ϕ . The view in the Rz plane shows a mix of bending and breathing motions. The disk is moving downward inside the Solar circle and upward outside the Solar circle and in addition it appears to be expanding away from the midplane. The generation of bending and breathing waves through internal disk dynamics and interactions with satellites such as the Sagittarius dwarf have been studied in N-body simulations by numerous authors including (Gómez et al. 2013; Chequers et al. 2018; Laporte et al. 2019; Poggio et al. 2021; Bennett et al. 2022) and Thulasidharan et al. (2022). Observational studies using data from various surveys in Widrow et al. (2012); Williams et al. (2013); Carlin et al. (2013); Carrillo et al. (2018); Katz, D. et al. (2019); Wang et al. (2019); López-Corredoira et al. (2020).

4.2 Velocity vectors

To aid our understanding of the velocity field we present velocity vector maps in three projections. Similar vector field maps were presented in Pearl et al. (2017) using data from LAMOST and, most

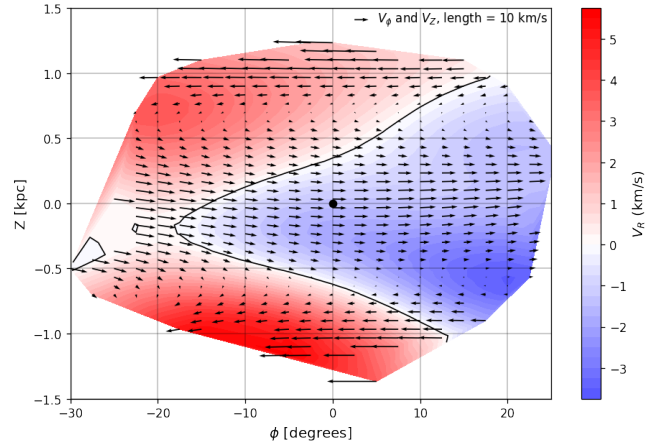


Figure 5. Map of the velocity field in $\phi - Z$ plane along a cylindrical surface at $R = 8.27$. Arrows represent the components V_ϕ and V_Z where, for clarity, we subtract 220 km s^{-1} from V_ϕ . The background color map shows V_R while black contour indicates the curve where $V_R = 0$.

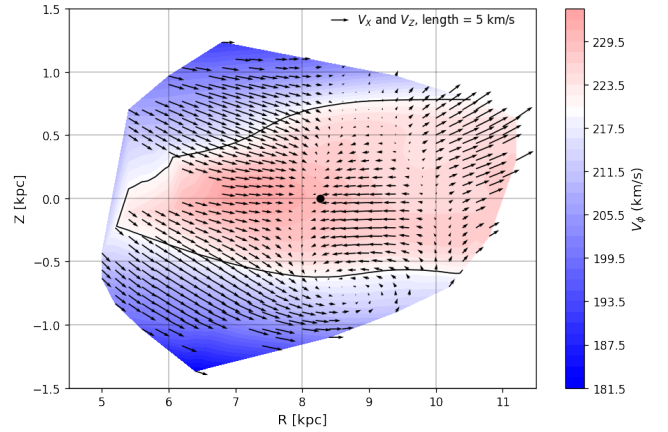


Figure 6. Velocity vector map in the RZ -plane for $\phi = 0^\circ$ with arrows representing V_R and V_Z . The background color map shows V_ϕ with the black contour indicating the curve where $V_\phi = 220 \text{ km s}^{-1}$.

recently, by Fedorov et al. (2022) using data from *Gaia* DR2. We begin with Figure 5, which presents the vector field in the ϕZ plane at $R = R_0$, that is, along a curved cylindrical surface that includes a part of the Solar circle. To help visualize the velocity field, we have subtracted off the vector $220 \text{ km s}^{-1} \hat{\phi}$. Radial velocities are shown as a color map. Thus, all three components of the velocity field are represented in the figure.

As already noted in the V_ϕ panel of Figure 6, the dominant feature of the map is the decrease in V_ϕ due to asymmetric drift as one moves away from the midplane. Velocities in the midplane are about 10 km s^{-1} higher than they are at $|Z| = 500 \text{ pc}$. Though the dominant flow is in the azimuthal direction, we do see a clear downward motion for $\phi < 0^\circ$, in agreement with Figure 7.

In Figure 6 we show the velocity field in the RZ -plane at $\phi = 0^\circ$, which passes through the position of the Sun. We see that there are three distinct regions defined primarily by the sign of V_R . Specifically, we find an inward flow centered on $(R, z) = (8.5, -0.2) \text{ kpc}$, an outward and downward flow inside the Solar circle, and an outward

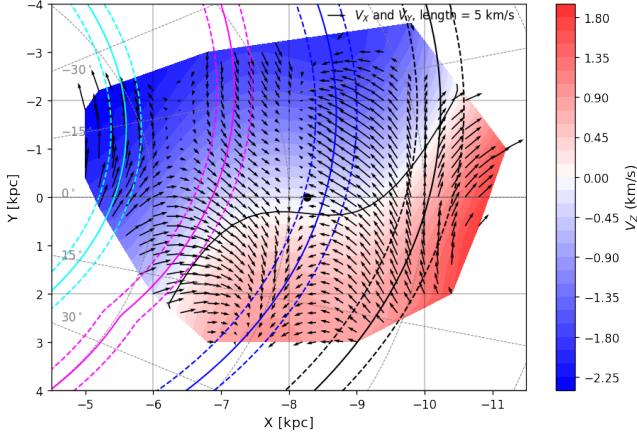


Figure 7. Velocity vector map in midplane. Arrows represent the V_X and V_Y components with the vector $230 \text{ km s}^{-1} \hat{\phi}$ subtracted for clarity. The background colormap shows V_Z and the black contour indicates the curve where $V_Z = 0$. Arcs show the model for nearby spiral arms from Reid et al. (2019). In order from the inner to the outer disc they are: Scutum (cyan), Sagittarius (magenta), Local Arm (blue), and Perseus (black).

and upward flow for $R > 10 \text{ kpc}$ and $z \sim 500 \text{ pc}$. The results are in good agreement with Figure 10 of Pearl et al. (2017) for regions where the samples overlap.

4.2.1 XY vectorfield

In Figure 7 we show the velocity field in the midplane with vertical bulk motions are shown as the background color map. The map paints an image of several flows in the vicinity of the Sun, which can be describe by a combination of expansion or compression and shear. For example, roughly along the Solar circle, we find radial compression and azimuthal shear — the dominant motion inside the Solar circle is outward and toward positive ϕ while the motion just beyond the Solar circle is inward and toward negative ϕ .

It is tempting to attribute flows in the midplane to the presence of spiral arms. With this in mind, we overlay the spiral arm model of Reid et al. (2019). In general, one expects to see motion toward the Galactic centre on the leading side of a spiral arm and motion away from the Galactic centre on the trailing side (Kawata et al. 2014; Grand et al. 2015; Hunt et al. 2015). This pattern is indeed seen along the Local Arm in Figure 7 though the connection between flows in our map and the other arms is more tenuous. For example, there is little evidence for changes in the velocity field along the Sagittarius arm. This may be because Sagittarius is a relatively minor arm of the Galaxy and mainly a region rich in star formation but having relatively little mass (Churchwell et al. 2009). Analysis of density enhancement (Benjamin et al. 2005) and Galactocentric rotation (Kawata et al. 2018) show few of the expected features for the other arms.

5 VELOCITY GRADIENT

In the previous section, we showed that our GP model could be queried to give the bulk velocity field \mathbf{V} at any position in the sample region. Since the GP solution is continuous and differentiable, we can also use it to infer the gradient of the velocity field, a 3×3 -tensor whose components are $\partial V_i / \partial X_j$. These components can be

computed either by replacing the kernel functions in Equations 12 and 13 with their gradients or by a finite difference scheme. We have confirmed that the two methods agree for the RBF kernel. In what follows we use finite differencing. Similar results are presented in Fedorov et al. (2021).

5.1 Oort constants

Gradients of the velocity field played a central role in Oort’s seminal work on the rotation of the Galaxy Oort (1927). The basic idea was to expand the velocity field near the Sun as a Taylor series in position. Though Oort considered only axisymmetric flows in the $X - Y$ plane, the method was extended to general three dimensional flows by Ogrodnikoff (1932); Milne (1935); Chandrasekhar (1942) and Ogorodnikov (1965).

To linear order in position, the velocity field near the Sun can be written as a Taylor series

$$\mathbf{V} = \mathbf{V}_\odot + \mathbf{H} \cdot \mathbf{x} + \mathcal{O}(x^2). \quad (20)$$

If we restrict ourselves to the projection of the velocity field onto the midplane of the Galaxy, then \mathbf{H} reduces to the 2×2 matrix

$$\mathbf{H} = \begin{pmatrix} \partial v_x / \partial x & \partial v_y / \partial x \\ \partial v_x / \partial y & \partial v_y / \partial y \end{pmatrix}_{\mathbf{x}=0} \equiv \begin{pmatrix} K + C & A - B \\ A + B & K - C \end{pmatrix}. \quad (21)$$

where the second equality defines the Oort constants A , B , C , and K . These constants measure, respectively, the azimuthal shear, vorticity, radial shear, and divergence of the velocity field in the midplane of the disk. In Galactocentric polar coordinates (R, φ) the Oort constants are given by

$$2A = \frac{v_\varphi}{R} - \frac{\partial v_\varphi}{\partial R} - \frac{1}{R} \frac{\partial v_R}{\partial \varphi} \quad (22)$$

$$2B = -\frac{v_\varphi}{R} - \frac{\partial v_\varphi}{\partial R} + \frac{1}{R} \frac{\partial v_R}{\partial \varphi} \quad (23)$$

$$2C = -\frac{v_R}{R} + \frac{\partial v_R}{\partial R} - \frac{1}{R} \frac{\partial v_\varphi}{\partial \varphi} \quad (24)$$

$$2K = \frac{v_R}{R} + \frac{\partial v_R}{\partial R} + \frac{1}{R} \frac{\partial v_\varphi}{\partial \varphi} \quad (25)$$

Chandrasekhar (1942).

The usual method for determining the Oort constants from astrometric data is based on the observation that the proper motion of a star in the direction of Galactic longitude, μ_l , and the line-of-sight velocity, v_{los} , can be expressed in terms of sine and cosine functions of l . The Oort constants appear as coefficients in this truncated Fourier series and can therefore be determined by standard statistical methods. (See, for example, Feast & Whitelock (1997); Olling & Dehnen (2003); Bovy (2017); Vityazev et al. (2018); Wang et al. (2021))

In this paper, we compute the Oort constants directly from our GP model for the velocity field using the above equations. Our results along with a selection of values from the literature are given in Table 2. We find excellent agreement with recent measurements from Bovy (2017); Vityazev et al. (2018); Li et al. (2019) and Wang et al. (2021). As noted above, the values from the literature all determine the Oort constants by fitting μ_l and v_{los} to a low-order Fourier series in l . They do, however, use data from different surveys and with different geometric selection functions and sample sizes. For example, both Bovy (2017) and Li et al. (2019) consider large samples of stars within 500 pc of the Sun. Bovy (2017) considers main sequence stars from the Tycho–Gaia Astrometric (TGAS) catalog (Michalik, Daniel et al. 2015) while Li et al. (2019) considers all stars from Gaia DR2.

Table 2. Comparison of measured values for the Oort constants from the literature and from this work in units of $\text{km s}^{-1} \text{kpc}^{-1}$. For the GP model we provide the inferred values at the exact position of the Sun and average values over a spherical volume of radius 500 pc.

Origin	A	B	C	K
Oort (1927)	~ 19	~ -24		
Feast (1997)	14.8 ± 0.8	-12.4 ± 0.6		
Olling (2003)	15.9 ± 2	-16.9 ± 2	-9.8 ± 2	
Bovy (2017)	15.3 ± 0.4	-11.9 ± 0.4	-3.2 ± 0.4	-3.3 ± 0.6
Vityazev (2018)	16.3 ± 0.1	-11.9 ± 0.1	-3.0 ± 0.1	-4.0 ± 0.2
Li (2019)	15.1 ± 0.1	-13.4 ± 0.1	-2.7 ± 0.1	-1.7 ± 0.2
Wang (2021)	16.3 ± 0.9	-12.0 ± 0.8	-3.1 ± 0.5	-1.3 ± 1.0
This work (p)	16.2 ± 0.2	-11.7 ± 0.2	-3.1 ± 0.2	-3.0 ± 0.2
This work (v)	15.2 ± 0.8	-12.4 ± 0.9	-2.9 ± 0.8	-2.3 ± 0.5

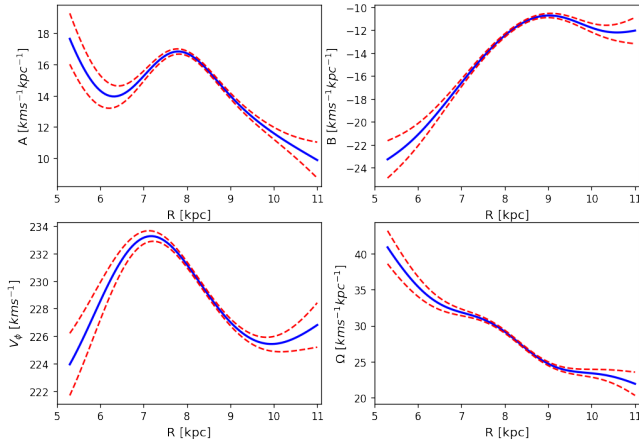


Figure 8. Galactic parameters as a function of radius. Top: Oort parameters A (left) and B (right). Bottom left: V_ϕ . Bottom right: Angular velocity $\Omega = A - B$. The model is queried along the line passing from the Galactic centre through the Sun. The red dashed lines show the 1σ uncertainties.

Wang et al. (2021) uses a relatively small sample of A -stars from LAMOST with a similar range in distance from the Sun. Finally, Vityazev et al. (2018) uses stars from TGAS but with the larger reach of 1.5 kpc.

Our model allows us to predict the Oort constants at a single point, namely the position of the Sun. These values are given in the second to last line in Table 2. To allow for a closer comparison to literature values, we also include values for the Oort constants averaged over a spherical volume of radius 500 pc.

5.2 Oort functions

In Oort's 1927 original work, stars are assumed to follow circular orbits in the midplane of the Galaxy. Under this assumption, C and K are identically zero and A and B can be written in terms of circular speed and its gradient at the position of the Sun. They therefore provide a direct probe of the gravitational potential and hence matter distribution in the Galaxy. Olling & Merrifield (1998) extended the idea of Oort constants to Oort functions with

$$A(R) = \frac{1}{2} \left(\frac{v_c(R)}{R} - \frac{dv_c}{dR} \right) \quad (26)$$

$$B(R) = -\frac{1}{2} \left(\frac{v_c(R)}{R} + \frac{dv_c}{dR} \right) \quad (27)$$

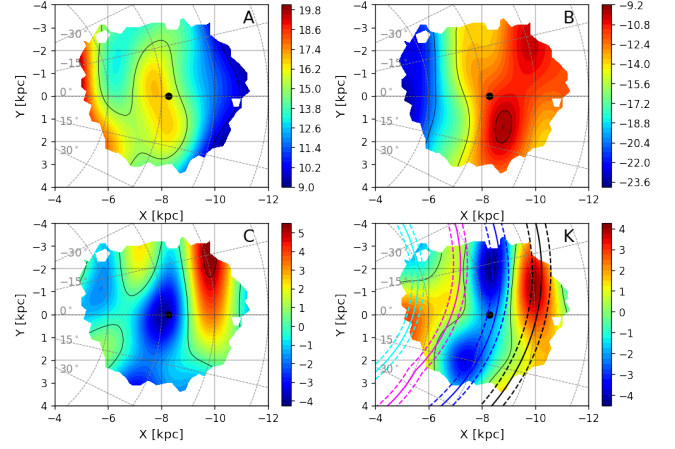


Figure 9. Oort constants A , B , C , and K calculated from Equations 22 – 25. Colormap units are in $\text{km s}^{-1} \text{kpc}^{-1}$. The spiral arms model of Reid et al. (2019) is also over-plotted for the local divergence (K). In order of inner to the outer disc the arms are: Scutum (cyan), Sagittarius (magenta), Local Arm (blue), and Perseus (black).

where v_c is the circular speed. They then derived $A(R)$ and $B(R)$ from mass models of the Milky Way and Oort constant measurements.

In Figure 8 we show $A(R)$ and $B(R)$ over the sample region. Note that our results for $A(R)$ and $B(R)$ use mean V_ϕ rather than v_c and therefore include the effects of asymmetric drift. Nevertheless, they show the same broad trends as seen in Olling & Merrifield (1998) and more recently, Fedorov et al. (2021). $A(R)$ is a decreasing function of R with a "bump" just inside the Solar circle. $B(R)$ is an increasing function of R . In the bottom panels of Figure 8 we show the rotation curve V_ϕ and angular velocity curve $\Omega = |A - B|$, which show departures from a flat rotation curve at the few km s^{-1} level.

The expressions for the Oort constants in Equations 22–25 can similarly be extended to function of R and φ to yield maps of Oort functions in the Galactic midplane. These are shown in Figure 9. Were the Galaxy in an axisymmetric steady state, we would find that $C = K = 0$ and A and B depend only on R . Though C and K are about a factor of five smaller than A and B they are clearly nonzero. Moreover, all four functions show variations in φ though the dominant gradients are in the R -direction. The prominent regions of shear (lower left panel showing C) and compression (lower right panel showing K) provide another way of visualizing the in-plane flows already seen in Figure 7.

5.3 Divergence of the velocity field

As mentioned above, the Oort constants are constructed from $X - Y$ derivatives of the in-plane components of the velocity field. More generally, \mathbf{H} in Equation 20 is a 3×3 tensor. This tensor can be written as the sum of a six-component symmetric tensor M^+ and a three-component anti-symmetric tensor M^-

$$M^\pm = \frac{1}{2} \left(\frac{\partial v_i}{\partial x_k} \pm \frac{\partial v_k}{\partial x_i} \right) \quad (28)$$

where as before, the components are evaluated at the position of the Sun (Ogorodnikoff 1932; Milne 1935; Ogorodnikov 1965; Tsvetkov & Amosov 2019; Fedorov et al. 2021). Note that the coefficients of M^\pm include the Oort constants. For example, $A = M_{12}^+$ and $B = M_{21}^-$.

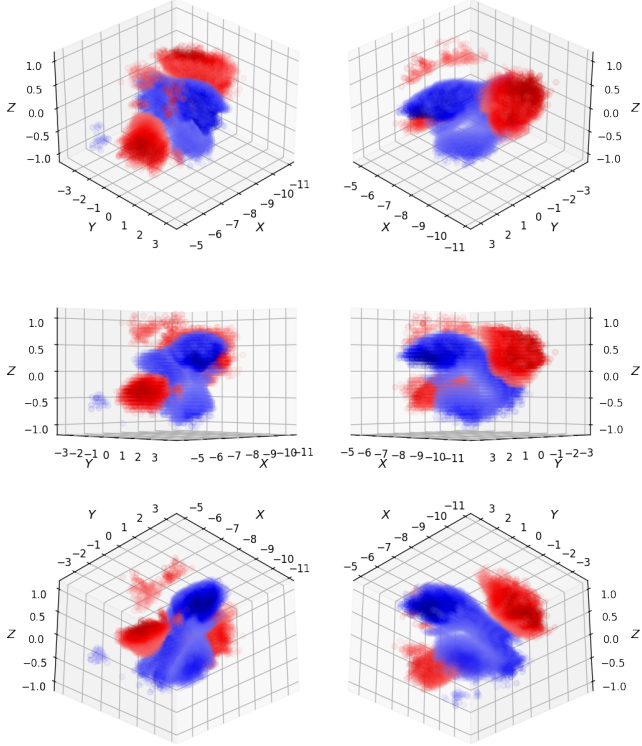


Figure 10. Divergence of the velocity field, calculated using cylindrical coordinates. Regions with $|\nabla \cdot \mathbf{V}| > 5 \text{ km s}^{-1} \text{ kpc}^{-1}$ are plotted, positive in red and negative in blue. Coloring and opacity is scaled with amplitude of the divergence.

Recently, the nine parameters of the velocity gradient method have been estimated using data from *Gaia* DR2 (Vityazev et al. 2018; Bobylev & Bajkova 2021).

Here, we focus on the divergence of the velocity field $\nabla \cdot \mathbf{V}$, which corresponds to the trace of M^+ . Recall that the zeroth moment of the collisionless Boltzmann equation yields the continuity equation

$$\frac{\partial \rho}{\partial t} + \nabla \cdot (\rho \mathbf{V}) = 0 \quad (29)$$

where ρ is the stellar density. This equation may be written as

$$\frac{1}{\rho} \frac{d\rho}{dt} = -\nabla \cdot \mathbf{V} \quad (30)$$

where $d/dt = \partial/\partial t + \mathbf{V} \cdot \nabla$ is the total derivative. Thus, a region of positive divergence indicates that either the stellar distribution is expanding, or stars are being transported into a region of lower density. Either way, $\nabla \cdot \mathbf{V}$ is a clear signal of disequilibrium in the disk.

In Figure 10 we show the divergence in three dimensions from six different viewing angles. We find a prominent region of negative divergence corresponding to compression in the velocity field running through the Solar Neighborhood and roughly aligned with Galactic azimuth. This is in good agreement with the results for K in the Galactic plane as seen in the lower-right panel of Figure 9. This region is bracketed by regions of positive divergence, one below the midplane and inside the Solar circle and the other above the midplane and outside the Solar circle. The amplitude of the diver-

gence is $5 - 10 \text{ km s}^{-1} \text{ kpc}^{-1}$, which implies that the time-scale for the logarithm of the density to change is of order $100 - 200 \text{ Myr}$.

6 DISCUSSION

Our discussion of the divergence of the stellar velocity field illustrates how a GP model can provide a link between theory and data. In particular, the divergence gives us a direct indication of regions in the disk where the *total* time derivative of $\ln \rho$ is nonzero. Clearly, if we have ρ itself, then we can estimate the convective derivative term $\mathbf{V} \cdot \nabla \rho$ and hence infer the *partial* time derivative of ρ . In this way, we gain information about time-dependent phenomena in the disk from a kinematic snapshot. Models of ρ for particular tracer populations require detailed knowledge of the selection function but are certainly accessible given the wealth of astrometric data available.

In a similar fashion, GP models for components of the velocity dispersion tensor would allow one to study the first moments of the CBE, namely the Jeans equations. In contrast with the continuity equation, these equations involve gradients of the gravitational potential. Thus, we will typically have two unknown quantities, one involving time-derivatives of the moments and the other involving the potential. Nevertheless, one should be able to infer something about the dynamics of the stellar disk, and in particular, departures from equilibrium by modelling moments of the DF via GP regression.

These considerations suggest an extension of the present work where we treat the output as a single three-components vector rather than three independent scalars. Doing so would allow for correlations between the different components of the velocity field. The framework for extending GP regression to vector outputs is already well-established (Alvarez et al. 2011).

7 CONCLUSIONS

In this paper, we present a GP model for the mean or bulk stellar velocity field in the vicinity of the Sun using astrometric measurements from *Gaia* DR2. The model is nonparametric in the sense that there are no prior constraints on the functional form of the velocity field. Instead, one specifies the functional form of the kernel function, which through a set of hyperparameters, controls properties of the prior on the velocity field such as its coherence length.

The main challenge in applying GP regression to *Gaia* data comes from the large- N requirements in both computing time and RAM. Fortunately, there is a large effort within the machine learning community on addressing these problems (See, for example, Hensman et al. (2013)). In this work, we have just started to exploit methods developed in that field.

Our model provides smooth, differentiable versions of the velocity field maps found in Katz, D. et al. (2019) and elsewhere. The *Gaia* maps used different binning schemes to compute different projections of the velocity field. In our case, we compute a single GP model (or more precisely, three independent models for each of the cylindrical velocity field components) from which properties of the velocity field could be derived. As a check of the model, we confirm that the values for the Oort constants derived by differentiating the velocity field agree extremely well with recent determinations in the literature.

A GP model for the velocity field can thus provide a starting point for making contact between astrometric data and dynamics via the continuity and Jeans equations. Already, our results for the divergence of the velocity field have provided a unique perspective on departures in the disk from an equilibrium state.

ACKNOWLEDGEMENTS

It is a pleasure to thank Dan Foreman-Mackey, Hamish Silverwood, and Lauren Anderson for helpful conversations on Gaussian processes. We acknowledge the financial support of the Natural Sciences and Engineering Research Council of Canada. LMW is grateful to the Kavli Institute for Theoretical Physics at the University of California, Santa Barbara for providing a stimulating environment during a 2019 program on galactic dynamics. His research at the KITP was supported by the National Science Foundation under Grant No. NSF PHY-1748958.

DATA AVAILABILITY

Data used in this paper is available through Zenodo (<https://doi.org/10.5281/zenodo.2557803>)

REFERENCES

- Alvarez M. A., Rosasco L., Lawrence N. D., 2011, arXiv e-prints, [p. arXiv:1106.6251](https://arxiv.org/abs/1106.6251)
- Bauer M., van der Wilk M., Rasmussen C. E., 2016, arXiv e-prints, [p. arXiv:1606.04820](https://arxiv.org/abs/1606.04820)
- Benjamin R. A., et al., 2005, *ApJ*, 630, L149
- Bennett M., Bovy J., Hunt J. A. S., 2022, *ApJ*, 927, 131
- Binney J., 2013, *New Astron. Rev.*, 57, 29
- Binney J., Tremaine S., 2008, *Galactic Dynamics: Second Edition*. Princeton University Press
- Bobylev V. V., Bajkova A. T., 2021, *Astronomy Letters*, 47, 607
- Bovy J., 2017, *MNRAS:Letters*, 468, L63
- Carlin J. L., et al., 2013, *ApJ*, 777, L5
- Carrillo I., et al., 2018, *MNRAS*, 475, 2679
- Chandrasekhar S., 1942, *Principles of stellar dynamics*. Dover Phoenix Editions
- Chequers M. H., Widrow L. M., Darling K., 2018, *MNRAS*, 480, 4244
- Churchwell E., et al., 2009, *PASP*, 121, 213
- Cui X.-Q., et al., 2012, *Research in Astronomy and Astrophysics*, 12, 1197
- Feast M., Whitelock P., 1997, *MNRAS*, 291, 683
- Fedorov P. N., Akhmetov V. S., Velichko A. B., Dmytrenko A. M., Denyschenko S. I., 2021, *MNRAS*, 508, 3055–3067
- Fedorov P. N., Akhmetov V. S., Velichko A. B., Dmytrenko A. M., Denyschenko S. I., 2022, arXiv e-prints, [p. arXiv:2205.09381](https://arxiv.org/abs/2205.09381)
- Frisk J. K. S., Schönrich R., 2019, *MNRAS*, 490, 5414
- GPpy since 2012, GPpy: A Gaussian process framework in python, [http://github.com/SheffieldML/GPy](https://github.com/SheffieldML/GPy)
- Gaia Collaboration et al., 2018, *A&A*, 616, A1
- Gómez F. A., Minchev I., O’Shea B. W., Beers T. C., Bullock J. S., Purcell C. W., 2013, *MNRAS*, 429, 159
- Grand R. J. J., Bovy J., Kawata D., Hunt J. A. S., Famaey B., Siebert A., Monari G., Cropper M., 2015, *MNRAS*, 453, 1867
- Hensman J., Fusi N., Lawrence N. D., 2013, *Proceedings of the Twenty-Ninth Conference on Uncertainty in Artificial Intelligence*, pp 282 – 290
- Hunt J. A. S., Kawata D., Grand R. J. J., Minchev I., Pasetto S., Cropper M., 2015, *MNRAS*, 450, 2132
- Johnson D. R. H., Soderblom D. R., 1987, *AJ*, 93, 864
- Jorge Nocedal S. J. W., 2006, *Numerical Optimization*. Springer, <https://doi.org/10.1007/978-0-387-40065-5>
- Katz, D. et al., 2019, *A&A*, 622, A205
- Kawata D., Hunt J. A. S., Grand R. J. J., Pasetto S., Cropper M., 2014, *MNRAS*, 443, 2757
- Kawata D., Baba J., Ciucă I., Cropper M., Grand R. J. J., Hunt J. A. S., Seabroke G., 2018, *MNRAS*, 479, L108
- Khanna S., Sharma S., Bland-Hawthorn J., Hayden M., 2022, arXiv e-prints, [p. arXiv:2204.13672](https://arxiv.org/abs/2204.13672)
- Laporte C. F. P., Minchev I., Johnston K. V., Gómez F. A., 2019, *MNRAS*, 485, 3134
- Li C., Zhao G., Yang C., 2019, *ApJ*, 872, 205
- López-Corredoira M., Garzón F., Wang H. F., Sylos Labini F., Nagy R., Chrobáková Ž., Chang J., Villarroel B., 2020, *A&A*, 634, A66
- Michalik, Daniel Lindegren, Lennart Hobbs, David 2015, *A&A*, 574, A115
- Milne E. A., 1935, *MNRAS*, 95, 560
- Ogorodnikov K. F., 1965, *Dynamics of stellar systems*. Pergamon Press
- Ogrodnikoff K., 1932, *Z. Astrophys.*, 4, 190
- Olling R. P., Dehnen W., 2003, *ApJ*, 599, 275–296
- Olling R. P., Merrifield M. R., 1998, *MNRAS*, 297, 943
- Oort J. H., 1927, *Bull. Astron. Inst. Netherlands*, 3, 275
- Pearl A. N., Newberg H. J., Carlin J. L., Smith R. F., 2017, *ApJ*, 847, 123
- Poggio E., Laporte C. F. P., Johnston K. V., D’Onghia E., Drimmel R., Grion Filho D., 2021, *MNRAS*, 508, 541
- Rasmussen C. E., Williams C. K., 2006, *Gaussian Processes for Machine Learning*. MIT Press, <http://www.gaussianprocess.org/gpml/chapters/RW.pdf>
- Reid M. J., et al., 2019, *ApJ*, 885, 131
- Roeser S., Demleitner M., Schilbach E., 2010, *AJ*, 139, 2440
- Sale S. E., Magorrian J., 2018, *MNRAS*, 481, 494
- Schönrich R., 2012, *MNRAS*, 427, 274
- Schönrich R., McMillan P., Eyer L., 2019, *MNRAS*, 487, 3568
- Sellwood J. A., 2013, in *Oswalt T. D., Gilmore G., eds., Vol. 5, Galactic Structure and Stellar Populations*. Springer Science, p. 923, [doi:10.1007/978-94-007-5612-0_18](https://doi.org/10.1007/978-94-007-5612-0_18)
- Steinmetz M., et al., 2006, *AJ*, 132, 1645
- Thulasidharan L., D’Onghia E., Poggio E., Drimmel R., Gallagher J. S. I., Swigum C., Benjamin R. A., Alves J., 2022, *A&A*, 660, L12
- Titsias M., 2009, *Journal of Machine Learning Research - Proceedings Track*, 5, 567
- Tsvetkov A. S., Amosov F. A., 2019, *Astronomy Letters*, 45, 462
- Virtanen P., et al., 2020, *Nature Methods*, 17, 261
- Vityazev V. V., Popov A. V., Tsvetkov A. S., Petrov S. D., Trofimov D. A., Kiyaev V. I., 2018, *Astronomy Letters*, 44, 236
- Wang H.-F., et al., 2019, *MNRAS*, 491, 2104
- Wang F., Zhang H.-W., Huang Y., Chen B.-Q., Wang H.-F., Wang C., 2021, *MNRAS*, 504, 199
- Widrow L. M., Gardner S., Yanny B., Dodelson S., Chen H.-Y., 2012, *ApJ*, 750, L41
- Williams M. E. K., et al., 2013, *MNRAS*, 436, 101
- Yanny B., et al., 2009, *AJ*, 137, 4377

This paper has been typeset from a \LaTeX file prepared by the author.